Evaluating vertically resolved Pandora formaldehyde retrievals using airborne and ground-based in situ measurements

Apoorva Pandey[1,2], Bryan K. Place[2,3], Thomas F. Hanisco[2], Jong-Uk Park[2], Elena S. Lind[2], Jason M. St. Clair[1,2], Erin R. Delaria[2,4], Glenn M. Wolfe[2], Ronaldo Lopez[5], Paul V. Zimba[5], K. Lee Thornhill[6]

[1]University of Maryland Baltimore County, Baltimore, MD, USA
[2]NASA Goddard Space Flight Center, Greenbelt, MD, USA
[3]SciGlob, Columbia, MD, USA
[4]University of Maryland, College Park, MD, USA
[5]Virginia Commonwealth University, Richmond, Virginia, USA
[6]NASA Langley Research Center, Hampton, Virginia, USA

Correspondence to: Apoorva Pandey (apoorva@umbc.edu)

Abstract. Pandora multi-axis retrievals in the boundary layer provide continuous observations of formaldehyde (HCHO) vertical distribution, yet validation of these retrievals against independent measurements remains limited. This work evaluates Pandora retrievals of the vertical distribution of formaldehyde (HCHO) against aircraft in situ measurements collected at four U.S. East Coast sites during the summers of 2024 and 2025. Across 31 collocated aircraft spirals, Pandora tropospheric columns agree with aircraft-integrated columns within measurement uncertainty, with residual discrepancies potentially linked to horizontal and vertical HCHO gradients insufficiently characterized by the airborne data. Comparison of retrieved vertical profiles with aircraft measurements reveals a systematic overconcentration of HCHO in the lowest operational retrieval layers. We show that this bias arises from interpreting the O_2–O_2-derived geometric proxy as a layer midpoint rather than an upper sensitivity bound and demonstrate that a revised height-mapping formulation removes it (near-surface difference ≤ 0.7 ppb) across all evaluated sites. These results support the use of Pandora HCHO observations for satellite column validation, and for constraining the vertical distribution of HCHO used in geostationary retrieval algorithms and atmospheric models.

1 Introduction

Formaldehyde (HCHO) is a key intermediate in the oxidation of volatile organic compounds (VOCs). Because HCHO is produced efficiently during VOC oxidation, its abundance provides insight into the spatial distribution and strength of hydrocarbon emissions as well as photochemical activity in the troposphere. Satellite and ground-based column HCHO observations constitute an important tool for constraining VOC emissions (Sfendla et al., 2026; Shim et al., 2005), estimating atmospheric oxidizing capacity (Liao et al., 2019; Travis et al., 2022; Wolfe et al., 2019), and understanding atmospheric chemistry, including via model evaluation (Harkey et al., 2021).

Ground-based observations support assessments and interpretations of satellite HCHO retrievals (De Smedt et al., 2021; Vigouroux et al., 2020). Instruments in the Pandonia Global Network (PGN)—Pandora spectrometers—provide column HCHO measurements (Cede, 2024; Herman et al., 2009; Spinei et al., 2018) that are widely used for validation of satellite products (Chi et al., 2025; Ortega et al., 2026; Park et al., 2026; Rawat et al., 2026) from missions such as Tropospheric Emissions: Monitoring of Pollution (TEMPO) (Szykman and Liu, 2023; Zoogman et al., 2017), the Geostationary Environment Monitoring Spectrometer (GEMS) (Choi, 2018), and Sentinel-5 Precursor / TROPOspheric Monitoring Instrument (TROPOMI) (Veefkind et al., 2012). In addition to total columns, Pandora instruments also retrieve lower tropospheric columns, near-surface mixing ratios, and vertically resolved profiles of NO_2 and HCHO using sky-scattered measurements in Multi-Axis Differential Optical Absorption Spectroscopy (MAX-DOAS) mode (Honninger, 2004). These boundary layer observations help bridge the gap between total column measurements and near-surface concentrations that are most relevant for air-quality applications. Vertically resolved retrievals also help constrain satellite retrieval errors arising from model based prior profile shape factors.

The profile retrieval technique implemented in the PGN differs from conventional MAX-DOAS inversion approaches. Typically, MAX-DOAS retrievals employ the optimal estimation approach (Frieß et al., 2019; Tirpitz et al., 2021), which involves full radiative transfer modeling to estimate photon path lengths and requires assumed a priori trace-gas profiles similar to satellite retrieval frameworks. Another class of retrievals, known as parameterized algorithms (Wagner et al., 2011) use pre-calculated lookup tables, as functions of a handful of independent parameters, for computational efficiency. In contrast, the PGN retrieval algorithm (Cede, 2024; Nowak, 2022), also referred to as the NASA real time algorithm in previous literature (Frieß et al., 2019; Tirpitz et al., 2021), uses an analytical formulation that derives vertical sensitivity information directly from measured differential slant column densities.

Comparisons with more computationally intensive MAX-DOAS inversion methods using both synthetic datasets (Frieß et al., 2019) and field observations (Tirpitz et al., 2021) have shown that PGN retrievals achieve comparable performance while requiring substantially less computational effort. The few existing column level comparisons with aircraft observations (Nowlan et al., 2018; Sebol et al., 2026) indicate that the retrievals perform well with respect to tropospheric columns. Recently, Sebol et al. (2026) used airborne in situ HCHO and NO_2 profiles to suggest that Pandora profile retrievals may be biased high near the surface and biased low at higher altitudes. The profile comparison result rests on a single true vertical spiral over the Pandora site at the Edwards Airforce Base, CA. They note that the four New York City-area flights are not well suited to evaluating Pandora performance, given limitations in aircraft vertical sampling and spatiotemporal alignment with the Pandora observations. A systematic multi-site evaluation of Pandora MAX-DOAS HCHO profile retrievals requires well-targeted in situ measurements. Particularly, spatial and vertical HCHO gradients need careful consideration when assessing the vertical attribution of remote-sensing slant columns.

In this study, we evaluate vertically resolved HCHO retrievals from Pandora MAX-DOAS observations using in situ measurements obtained during recent airborne and ground-based field campaigns. The analysis uses data collected during the Student Airborne Research Program (SARP) field campaigns in 2024 and 2025 and the Associating Local Emissions of trace Gases with Regional Observations from Satellites (ALEGROS) campaign in 2024. These campaigns conducted repeat aircraft spiral profiles within the Pandora viewing sectors at multiple sites, providing collocated in situ vertical distributions of HCHO in the lower troposphere across a range of boundary layer conditions. The resulting dataset, spanning four sites along the U.S. East Coast, enables a systematic assessment of Pandora MAX-DOAS HCHO profile retrievals that no prior study has been positioned to conduct.

Using this dataset, we assess the consistency between Pandora-derived tropospheric columns, near-surface concentrations, and vertically resolved mixing ratios and the corresponding in situ measurements. This comparison reveals a systematic bias in the operational vertical layer mapping that concentrates retrieved HCHO into the lowest retrieval layers; we introduce a revised mapping formulation that resolves this bias and substantially improves agreement with in situ profiles.

2 Methods

2.1 Pandora instrumentation and retrieval approach

Each Pandora unit records direct sun and sky-scattered spectra between roughly 290–540 nm using a Czerny–Turner spectrometer with a ~0.6 nm full-width at half maximum resolution and ~0.13 nm pixel. In MAX-DOAS mode, profiling sequences of up to 15 elevation angles occur within ~10 min. Low elevation or high pointing zenith angles (PZAs: typically, 80° - 89°) are scanned at 1° intervals. Certain instrument sites have dark and/or reflective obstructions at the 89° viewing zenith angle, in which case the largest zenith angle in the sequence may be capped at 88° or 87°. For instruments included in this analysis, the largest zenith angle scanned was always 89°.

For MAX-DOAS observations, light path length through the boundary layer scales roughly as 1/sin(elevation) in the simple geometric approximation, with longer travel through lower atmospheric layers at lower elevation angle (Honninger, 2004; Wagner et al., 2004). Near-horizon angles maximize near-surface sensitivity, while lower zenith (higher elevation) angles behave close to geometrically. Scans at higher elevations, namely 75° and 60°, constrain the column abundance in the lower troposphere, since their slant path lengths can be well described using an ‘air gas’ proxy. While the column amounts are reported as ‘tropospheric columns’ in PGN ‘rfuh5’ Level 2 data files, the upper bound of the vertical sensitivities of MAX-DOAS observations is typically 3-4 km. Zenith observations serve as references for

differential slant-column retrievals. Operational measurement schedules for Pandoras also include short MAX-DOAS scans, which involve observations at 0°, 60°, 75° and near-horizon angles, and provide lower tropospheric column loading and near-surface mixing ratios. For the campaign period, all instruments, except for Pandora 75 at Essex, MD, operated on customized schedules that focused on profile scans, interspersed with short MAX-DOAS scans and direct sun measurements. Pandora 75 operated on a standard PGN measurement schedule during ALEGROS 2024.

Slant-column densities (SCDs) for HCHO and the air-mass indicator O_2–O_2 (oxygen collision-induced absorption) are obtained via DOAS fitting. For each sky scan sequence, zenith observations serve as a reference: strictly speaking, the slant columns are differential slant column densities (dSCDs) relative to zenith. The rfuh5 fitting setup used a 328.5–359 nm wavelength range. For this work, a modified fitting window (328.5–365 nm) was used to capture the stronger O_2–O_2 absorption band in the UV. This translated into lower noise and higher precision in O_2–O_2 slant columns, thus reducing the uncertainty in retrieved tropospheric columns and surface concentrations (see Fig. S1). The revised fitting window yields HCHO dSCDs consistently ~2% larger than the operational window (revised vs. operational ordinary least squares slope = 1.02, intercept =0, R^2 = 0.99). Expectedly, the effect on O_2–O_2 dSCDs is larger and more scattered with a revised vs. operational slope = 0.96 and R^2 = 0.69. Crucially, O_2–O_2 fit uncertainty is reduced by roughly 80% at every site-day. This referencing makes Pandora MAX-DOAS retrievals largely insensitive to drifts in wavelength registration and slit resolution. Vertical column densities (VCDs), near-surface mixing ratios and vertical profiles are obtained from dSCDs using the NASA real time algorithm.

A schematic of the PGN MAX-DOAS profile retrieval approach is shown in Fig. 1. Full equations corresponding to each retrieval step are available in Cede (2024) and are briefly explained in Appendix A. Rather than inverting measured dSCDs through a full radiative transfer model, the algorithm uses O_2–O_2 as a direct observational proxy for effective photon path length (Sinreich et al., 2013; Wagner et al., 2004). This is feasible because the vertical distribution of O_2–O_2 is well-constrained by air density and measured O_2–O_2 dSCDs encode information about where in the atmosphere photons are scattered and how far they travel. Normalizing trace gas dSCDs by the O_2–O_2 dSCD then partially cancels unknown radiative transfer effects, enabling column and profile estimates without an explicit forward model. The structural framework of this algorithm is physically motivated by single-scattering geometry. It also utilizes empirical formulations of aerosol (Appendix A, Eq. A8) and cloud corrections (Appendix A, Eqs. A11 and A12) that were evaluated against radiative transfer simulations during algorithm development and are treated here as fixed.

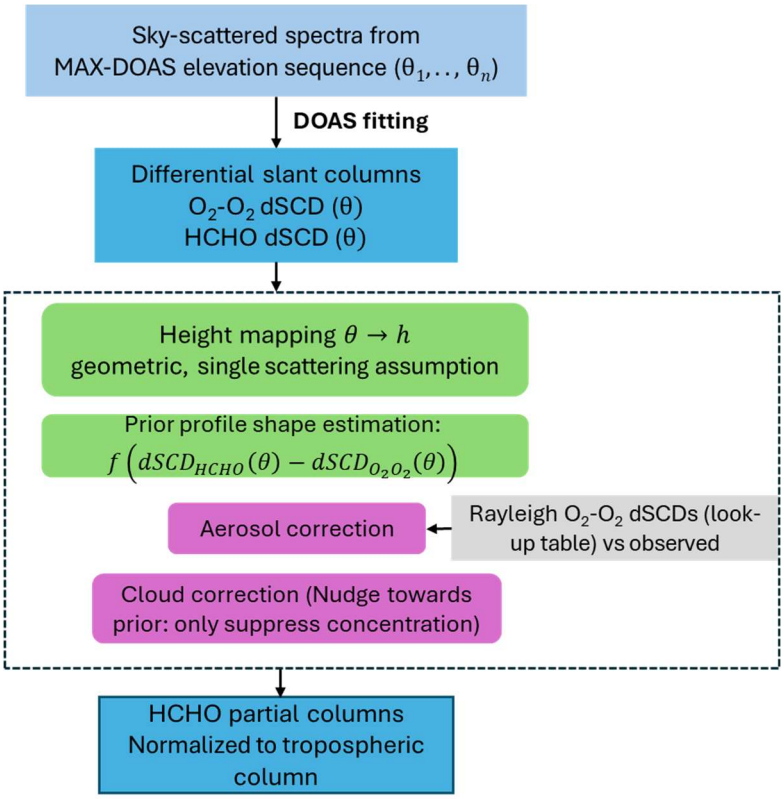


Figure 1. Schematic overview of the PGN MAX-DOAS profile retrieval algorithm. Retrieval steps are color-coded: green indicates analytical derivation grounded in single-scattering geometry; purple indicates empirical correction functions.

2.1.1 Height mapping

The equations described in this section use O_2–O_2 as a proxy for effective sensing height for each PZA scanned. The absolute surface density and vertical column for O_2–O_2 are derived climatologically — $n_{O_2O_2}^{surface}$ from station pressure/temperature via the ideal gas law, and $VCD_{O_2O_2}$ as that surface density times a COSPAR International Reference Atmosphere (CIRA) climatology (Rees et al., 1990) effective height for O_2. Then the observed O_2–O_2 dSCDs at each elevation angle are rescaled into an absolute air-mass equivalent. As shown in Fig. 1, each elevation angle (θ) in the scan sequence is mapped to a vertical atmospheric layer. Layer centers are defined as half the inferred geometric vertical extent of the mean photon path.

$$h_{mid}(\theta) = \frac{1}{2}\frac{dSCD_{O_2O_2}(\theta)+VCD_{O_2O_2}}{n_{O_2O_2}^{surface}}\cos(\theta) \quad (1)$$

Layer boundaries are then placed midway between adjacent layer centers (Fig. 2):

$$h_{top,i} = \frac{h_{mid,i}+h_{mid,i+1}}{2} \quad (2)$$

The topmost layer top is simply set to the highest layer center. The number density per layer multiplied by the layer width provides partial columns per layer, which are then scaled by the independently retrieved tropospheric vertical column density.

This mapping implicitly assumes that the vertical sensitivity kernel for a given elevation angle is symmetric about its midpoint and that contributions above and below this height are approximately balanced. However, MAX-DOAS sensitivity kernels are strongly asymmetric and bottom-weighted, with most sensitivity concentrated near the surface and a long, weak tail extending to higher altitudes (Frieß et al., 2006; Wagner et al., 2007). Interpreting the geometric proxy as a center height effectively creates strongly overlapping layers associated with low elevation angles. As demonstrated in Section 3.3, this leads to overweighting the contribution of atmospheric layers between 100 m and 1 km to the boundary layer column, resulting in systematic accumulation biases in trace gas loading when column normalization is enforced.

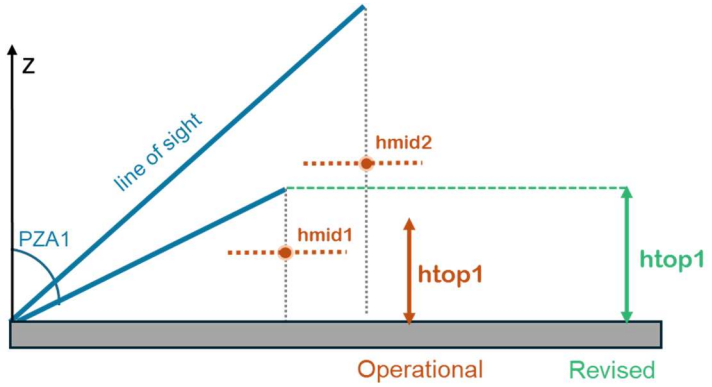


Figure 2. A schematic representation of the mapping between pointing zenith angles and atmospheric layer heights as calculated in the operational and the revised implementations.

To address this, an alternative height mapping scheme is presented here, which treats the inferred vertical path length as the cumulative altitude range sampled by photons contributing to the measurement. In this formulation, each elevation angle contains the integrated contribution from the surface up to h_{top}, and the vertical profile is constructed from the marginal information between successive cumulative sensitivity envelopes. The layer boundary corresponds to an effective upper sensitivity bound:

$$h_{top}(\theta) = \frac{dSCD_{O_2O_2}(\theta) + VCD_{O_2O_2}}{n_{O_2O_2}^{\text{surface}}} \cos(\theta) \qquad (3)$$

Empirical comparison with collocated in situ profiles (Section 3.3) demonstrates that this reinterpretation reduces systematic profile shape mismatch in near-surface layers observed under the h_{mid} formulation. Further, the column closure enforced in the algorithm (final step in Fig. 1; Appendix A) ensures that once the measurement sensitivity is appropriately distributed within the lower layers — where most of the retrievable information resides — the remaining column can be allocated to higher altitudes without introducing significant errors in the overall profile shape. It should be noted that the number of scan angles (and therefore, output layers) does not reflect the true degrees of freedom in the retrieved profile. A full treatment of the information content in the observations used here is beyond the scope of this work, but we emphasize that profiles should be interpreted as representing coarse boundary-layer structure.

2.1.2 Data quality filtering

All instruments used in this study were intensively monitored prior to and during the intercomparison period to ensure good performance (e.g., thermal stability, clean field of view, low humidity). The goal of quality filtering then was to eliminate cloud/haze contaminated observations. We screened this dataset using the normalized root mean square of the spectral fitting residual (wrms) and column/surface relative

uncertainties, rather than the operational L2 quality flag. The operational flag is set for consistency across the whole PGN network; this comparison instead calls for thresholds suited to a single campaign and a small set of sites, so we filter directly on two relevant diagnostics the inform the flag itself. The following thresholds were used to obtain a filtered dataset: (1) wrms < 0.0014. This threshold was the median fitting residual across the instruments in this study, only during the campaign period. (2) Relative uncertainty in the tropospheric column < 30%. (3) Relative uncertainty in the surface mixing ratio < 30%. The third criterion only applies to full profiles, while valid tropospheric column data only need to satisfy the first two criteria. Here, wrms serves as the primary filter because it is the most direct measure of how well the fitted model reproduces the observed spectrum, and thus, screens out spectrally contaminated retrievals. A useful wrms threshold should be of the order of the typical atmospheric optical depths relevant to the measurement (~0.002 in this study). Relative uncertainty serves as a secondary precision threshold, screening out retrievals too noisy to support a meaningful Pandora–aircraft comparison even when the fit itself is formally acceptable. Rawat et al. (2025) apply a related logic using wrms and absolute column uncertainties, but with loose thresholds set to maximize data availability across the network rather than to isolate the highest-quality subset for cross-comparison and validation.

2.2 Campaign overview

Data from four PGN sites—with multiple aircraft spirals at each location—were used in this study. Site names are listed in Table 1 and hereafter, the short names specified in the table will be used to refer to the Pandora sites. During ALEGROS (2024) and SARP-East (2024, 2025) field campaigns, the Dynamic Aviation King Air B200 aircraft performed spiral ascents/descents over each site, with an in situ payload measuring HCHO, NO_2, O_3, CH_4, CO_2 and geolocation and meteorological parameters. HCHO mixing ratios were measured at 1 Hz using the Compact Airborne Formaldehyde Experiment (CAFE) instrument (St. Clair et al., 2019) which has a precision of 100 ppt/s, a calibration uncertainty of 20% and an offset uncertainty of 100 pptv. Navigation data and static temperature and pressure were measured by the NASA Turbulent Air Motion Measurement System (TAMMS) instrument (Barrick et al., 1996). At the RRC site, an Aeris MIRA Ultra instrument (https://aerissensors.com/products/mira-ultra/), which has a nominal precision of 1 ppb/ 20 s and low thermal drift, was collocated with Pandora 31 to measure the local HCHO concentration at the surface.

Calibration of the CAFE instrument was performed both before and after each set of research flights using the techniques described in St. Clair, et al., 2019, with final data using the average of the two calibrations. Data quality control utilizes both instrument engineering data and data processing fitting metrics. The Aeris instrument (for measurement technique and calibration discussion, see Mouat et al., 2024; Shutter et al., 2019) was calibrated prior to the 2024 deployment and between 2024-2025 using dynamic dilution of an HCHO standard, with calibrated flow measurements. The HCHO standard concentrations are independently checked and updated prior to instrument calibration. No change was noted in the calibration coefficients. During field operation, the instrument was zeroed using DNPH cartridges (LpDNPH S10L cartridge, Sigma-Aldrich), at its default duty cycle of 15 s. The frequent zeros minimize drifts and background effects.

Spiral locations were chosen to be in the Pandora line of sight whenever possible. Pandora MAX-DOAS scans within ±10 min of each aircraft spiral were retained for comparison for all sites other than Essex, MD, where the time coincidence criterion was relaxed to ±30 min (since the operational measurement schedule did not provide profiles at the required cadence). After filtering Pandora data to meet the quality thresholds defined above, a total of 30 aircraft spirals were used for column comparisons and a subset of 26 were used in profile comparisons.

Table 1: Summary of PGN sites and aircraft spiral comparisons used in this study. "No. of spirals" gives the total collocated spiral count retained after quality filtering; values in parentheses indicate the subset with valid profile retrievals used in Sect. 3.3.

Site name	Short name	Pandora #	No. of spirals (valid profiles)
Rice River Center, Charles City, VA	RRC	31	8 (8)
Wallops Island, VA	Wallops	40	4 (4)
Essex, MD	Essex	75	16 (11)
Chesapeake Bay Bridge Tunnel, Virginia Beach VA	CBBT	255	3 (3)

2.3 Data analysis

For profile comparisons, aircraft measured pressure and temperature were used to convert Pandora partial columns (mol m^{-2}) to volumetric mixing ratios (ppb). For each comparison, aircraft profiles were vertically smoothed into 200 m bins. Means and standard deviations were calculated on a regular 200 m height grid. If a Pandora instrument performed time-coincident sky scans at multiple azimuths, only scans directed toward the spiral location were used. Each profile was resampled to a regular height grid with 200 m spacing using linear interpolation.

Volumetric HCHO mixing ratios from CAFE were converted to molecules m^{-3} units for calculating integrated columns. Profiles were extended from the lowest altitude sampled by the aircraft to the Pandora station altitude by linear interpolation between the lowest aircraft observation and a surface concentration observation. For the RRC site, the surface concentration was measured by the in situ Aeris instrument. For all other sites, Pandora near-surface observations were used.

Modeled wind fields from the High-Resolution Rapid Refresh (HRRR) model (Dowell et al., 2022) were used to support analysis for the RRC site. Hourly analyses (0 h forecast) from the 3 km contiguous United States HRRR grid were extracted at the native grid cell nearest RRC (37.326°N, 77.206°W), using 10 m and 950 mb wind fields accessed via the Herbie Python package (Blaylock, 2024)

3 Results and Discussion

3.1 HCHO column and its diurnal evolution

The availability of surface measurements at RRC, along with aircraft spirals aligned with the Pandora SE line of sight, enables an assessment of all Pandora MAX-DOAS data products at this site: tropospheric columns and column top heights (based on O_2-O_2 geometric path), near-surface concentrations and vertical profiles. In 2024, all six spirals were flown SE relative to the Pandora since the aircraft can sample down to an altitude of ~150 m over water. Figure 3a shows agreement between Pandora tropospheric columns and integrated in situ columns (n = 6 spirals), when the Pandora viewing direction aligns with the spiral location (shown in Fig. 3b). These observations highlight the importance of sampling geometry when comparing Pandora observations with in situ measurements (Fig. 3 and *Supporting Information*, Fig. S2). If the default MAX-DOAS azimuth for the Pandora at this site was towards southwest, discrepancies between Pandora and in situ columns would be up to a factor of two.

The SE viewing sector at RRC looks out over vegetated, undeveloped land, while the SW sector points toward the industrialized city of Hopewell. The two sectors are likely associated with their own

characteristic mix of VOC emissions, leading to spatial HCHO gradients under the right wind and photochemical conditions. HRRR 950 mb (~500 m AGL) wind fields on 06/25/2024 (fig. 3c), show weak, easterly morning winds that likely allow the SE/SW asymmetry to persist. By afternoon, winds organize into a moderate south-southwesterly flow, and the HCHO column gradient weakens and reverses sign.

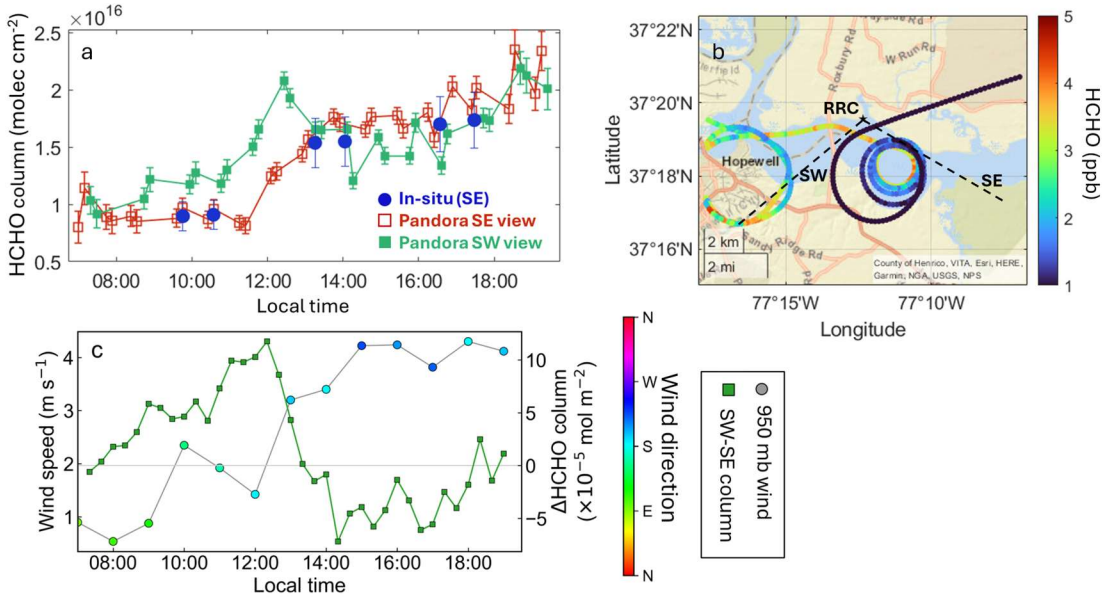


Figure 3. (a) Diurnal variation in HCHO boundary layer column on 06/25/2024 as captured by integrated columns from in situ aircraft observations over RRC and Pandora 31 tropospheric columns (with L2 independent uncertainty) observed in southeast and southwest viewing directions. (b) A map depicting the Pandora location and its line-of-sight along the two viewing directions (dashed line). Overlaid are airborne formaldehyde measurements over the area, including the first spiral of the day. (c) Diurnal variation in 950 mb wind speed and direction from HRRR overlaid with SW-SE HCHO column gradient from Pandora.

Across all sites, Pandora tropospheric HCHO columns agree with aircraft-derived columns, with most of the data in Fig. 4 falling close to the 1:1 line with a Pearson correlation coefficient of 0.89. Uncertainties due to extending the in situ profiles to the surface are as high as 50% when the lowest altitude of the spiral is over ~500 m. The lowest spiral altitude explains a significant portion of the divergence between Pandora and in situ column but as shown in Fig. 3, there can be significant horizontal heterogeneity in HCHO. Therefore, without knowledge of the three-dimensional HCHO fields, discrepancies between in situ and Pandora observations cannot be definitively classified as biases. With that caveat, Theil-Sen regression estimates are also shown in Figure 4. Considering all spiral comparisons (N = 31), Pandora tropospheric columns and integrated aircraft columns are related by $y = 0.779x + 3.60\times10^{15}$. Restricting to spirals whose lowest sampled altitude was ≤ 500 m (N = 25) gives $y = 0.820x + 2.90\times10^{15}$. Excluding the Essex, MD spirals — where HCHO profiles show strong vertical gradients in the lowest ~1km (see Fig. S4) that the aircraft spirals may not fully resolve — the remaining sites (N = 15) show closer to 1:1 agreement ($y = 1.058x - 2.29\times10^{15}$). We interpret the larger scatter at Essex as reflecting sampling/representativeness limitations specific to that site rather than systematic bias in the Pandora retrieval.

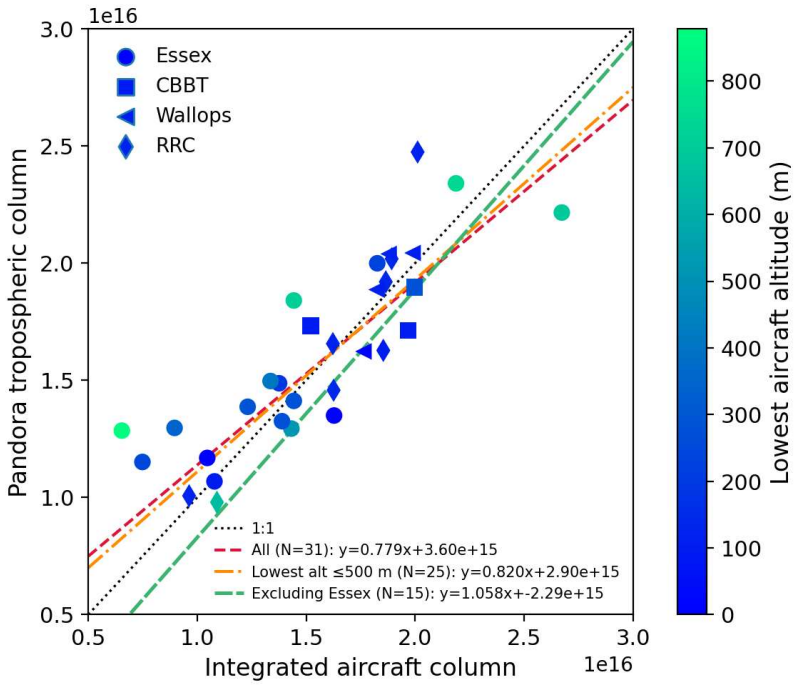


Figure 4. Pandora tropospheric columns versus integrated columns from in situ aircraft observations for all aircraft spirals (n=31) valid for comparison. The four comparison sites are denoted by different shapes. Datapoints are shaded by the lowest altitude sampled by the aircraft during a given spiral. The dotted black line is 1:1, while colored dashed lines show regression results.

3.2 Near-surface HCHO concentrations

Figure 5 compares near-surface HCHO mixing ratios retrieved by Pandora 31 at the RRC site with collocated Aeris measurements for all deployment days in 2024 and 2025. Pandora observations are shown for two viewing directions, while the in situ instrument provides a point measurement at the Pandora location. As with tropospheric column comparisons, spatial variability influences agreement between the two datasets. On three of the six days (Fig. 5a, b, and e), the in situ measurements closely track the Pandora near-surface concentrations retrieved in the southeast viewing direction. On two additional days (Fig. 5d and f), the in situ observations instead show stronger agreement with the Pandora southwest retrievals. Figure 5c shows one example where the Pandora and in situ measurements exhibit somewhat different diurnal behavior, suggesting that the Pandora observations were influenced by air masses that differed from those sampled at the instrument location. Supporting surface wind data are shown in Fig. S3—they indicate that significant SW-SE gradients in surface HCHO are typically associated with low wind speeds and/or north-south wind direction, which stratify the two sectors.

Taken together, these comparisons indicate that when the Pandora viewing direction samples air masses similar to those present at the instrument location, the retrieved near-surface HCHO mixing ratios agree well with the in situ measurements. Several aspects of the RRC site likely contribute to this strong agreement. The in situ sampling inlet is located at approximately the same height as the Pandora instrument and in an open environment with minimal nearby obstructions. In addition, the dominant horizontal gradients during the observed periods appear to occur along an east–west axis, which can be effectively sampled by the two Pandora viewing directions given the unobstructed lines of sight. Conversely, this highlights an important limitation when comparing Pandora retrievals with surface in situ monitors: Pandora measurements integrate scattered sunlight along horizontal paths extending several kilometers from the instrument. Horizontal extents for all observationa across the sites in this study ranged 9.5-13.3

km, with a median near 11 km. As a result, agreement with a single surface monitor will depend on the spatial structure of the trace gas field and the alignment of the viewing geometry with local gradients. This consideration becomes even more important for species such as NO_2, which typically exhibit stronger spatial heterogeneity near emission sources.

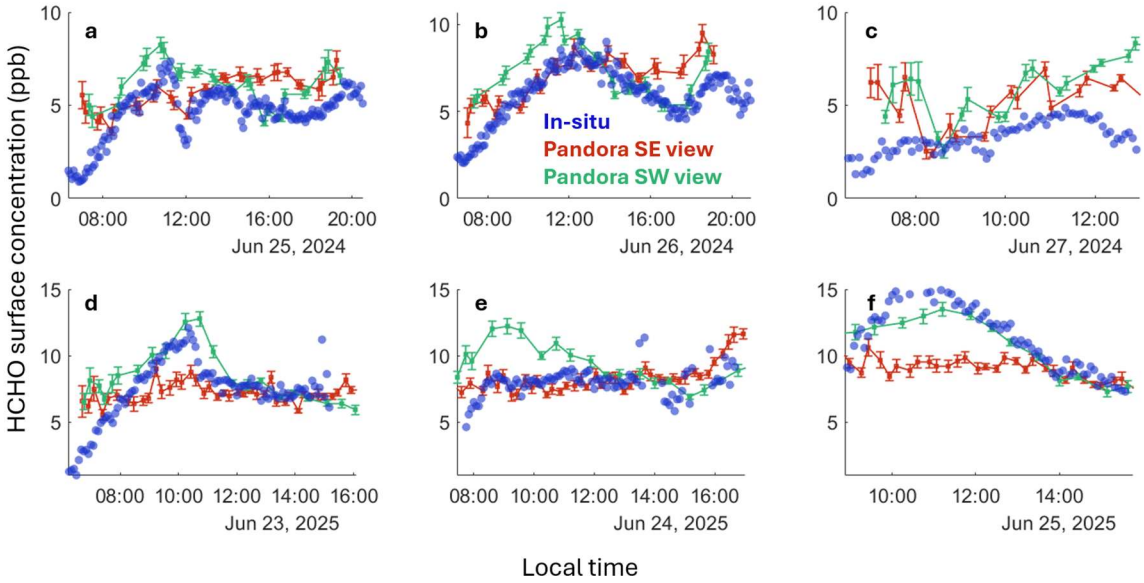


Figure 5. Diurnal variation in HCHO near-surface concentrations observed in 2024: (a) 06/25, (b) 06/26, (c) 06/27 and 2025: (d) 06/23, (e) 06/24, (f) 06/25. Pandora #31 near-surface observations in southeast and southwest viewing directions are shown (with the L2 independent uncertainty as error bars) along with in situ measurements at the RRC Pandora site.

3.3 Vertical structure

To evaluate the ability of Pandora MAX-DOAS retrievals to capture the vertical distribution of HCHO, retrieved profiles are compared with aircraft in situ measurements obtained during spiral ascents and descents conducted near each Pandora site. Figure 6 shows profile comparisons at the RRC site from the 2024 flights. On 06/25, three flights included two spirals each within the Pandora southeast line of sight. The aircraft observations were extended downward from the lowest aircraft altitude using the in situ surface mixing ratio from the ground site. For each spiral, two Pandora profiles were within the comparison window. Each panel shows the aircraft in situ profile alongside retrievals from the operational rfuh5 dataset (operational Pandora layer mapping and fitting window), and the revised height-mapping approach applied to spectral fits using the modified fitting window. Other permutations of fitting window and height mapping were tested but are omitted here for visual clarity, because the effect of the fitting window on the profile shape was much smaller than the height mapping.

The revised height mapping better captures the shape of the observed vertical distribution, including the near-surface enhancement and the gradient through the boundary layer. The operational mapping, by contrast, concentrates retrieved mixing ratios into the lower layers — a consequence of the way layer boundaries cluster near the surface when defined as midpoints between sensitivity centroids. This produces a vertical shape that bulges out in the first few 100 m above the surface and drops to very low values above ~1 km. This provides the motivation for the revised formulation adopted here. One profile comparison in Fig. 6 (panel f) shows a marked difference between the modified Pandora profile and the aircraft measurements. This seems to be largely a consequence of differences in the integrated column, rather than of profile shape attribution. Figure 3 shows that Pandora column observations in the southeast direction

exhibit a fluctuating behavior starting ~16:30 local time, with some data points higher than the aircraft-based column. Pandora near-surface concentrations (Fig. 5) at this time were also larger than the local in situ measurement. This may be due to spatial gradients in HCHO along the Pandora line of sight.

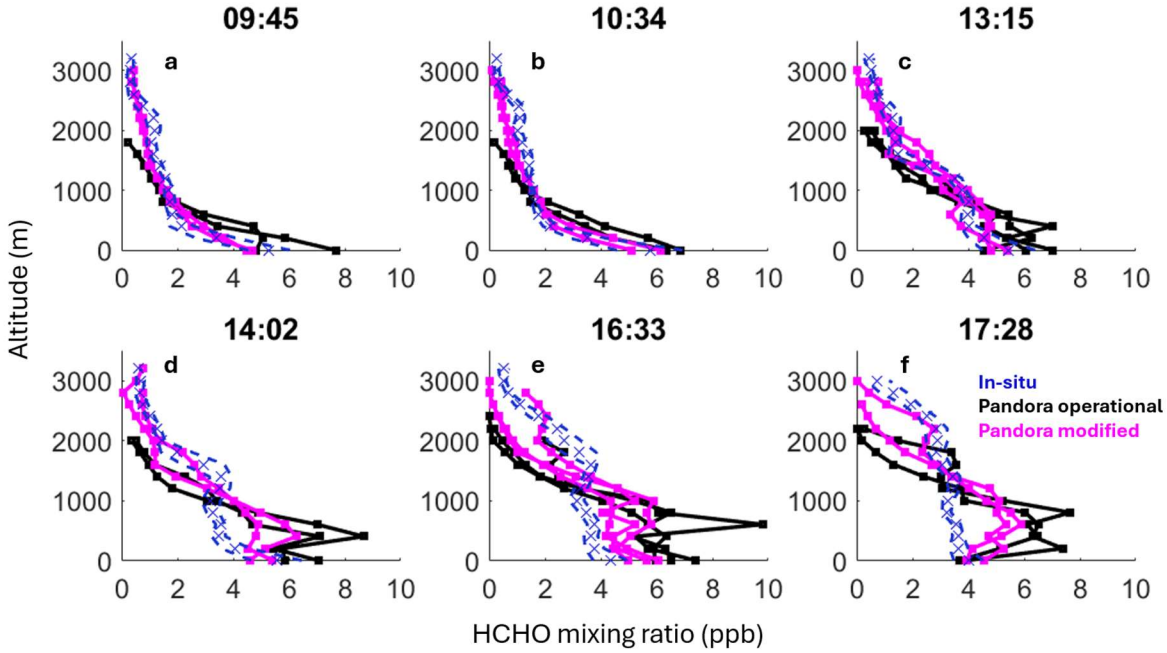


Figure 6. HCHO vertical profiles at RRC (Charles City, VA) on 06/25/2024 for morning (panels a and b), near-noon (panels c and d), and afternoon spiral (panels e and f) pairs. Each panel is labeled with the midpoint of the spiral time (local). Aircraft in situ measurements are shown as means (blue crosses) bounded by two standard deviations (dashed blue lines). Aircraft profiles are extended to the surface using the in situ near-surface mixing ratio from this site. Pandora retrievals using the operational layer mapping (black) and the revised height mapping (magenta) are shown.

The consistency between retrieved and observed vertical shapes is broadly reproduced across the full set of campaign sites. Given the largest number of collocated profile comparisons at Essex (n = 11), this site provides sufficient sampling to characterize the median profile shapes and their variability. Figure 7 shows a summary of these comparisons. The relatively narrow range of the (blue-shaded) in situ measurements below 1 km reflects the limited number of aircraft profiles extending to low altitudes at this site. Individual profiles from Essex are included in the Supplement (Fig. S4). Profile comparisons at Wallops (P40), CBBT (P255), and additional RRC flights are also provided (Figs. S5–S8). Across these comparisons, the revised mapping generally captures the shape of the observed boundary-layer profiles. The degree of agreement reflects both the vertical sensitivity of the retrieval and the degree to which the Pandora viewing direction samples air masses representative of the spiral location.

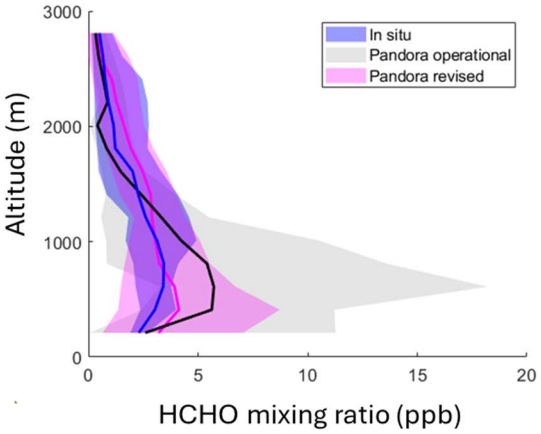


Figure 7. Medians (solid lines) and minimum-maximum ranges (shaded areas) of HCHO vertical profiles at Essex, MD from n=11 profile comparisons between 06/17/2024 and 06/22/2024. Pandora observations below the lowest flight altitude are not shown here. Single profiles are shown in Fig. S4.

For the two site-years (shown in the figures above) with a significant number of spirals, per-layer mean Pandora−aircraft differences, along with standard errors of the mean (SEM) are shown in Fig. 8. Under the operational mapping, both sites show retrievals exceeding the in situ measurement by roughly 2 ppb below ~800 m, with correspondingly lower HCHO abundance between ~1000–2000 m. This confirms the signature of HCHO being over-concentrated into the lowest retrieval layers (Sebol et al., 2026). Under the revised mapping, the mean difference is close to zero across the full sampled height range at both sites (largest remaining difference: 0.7 ppb, 500–1000 m at RRC).

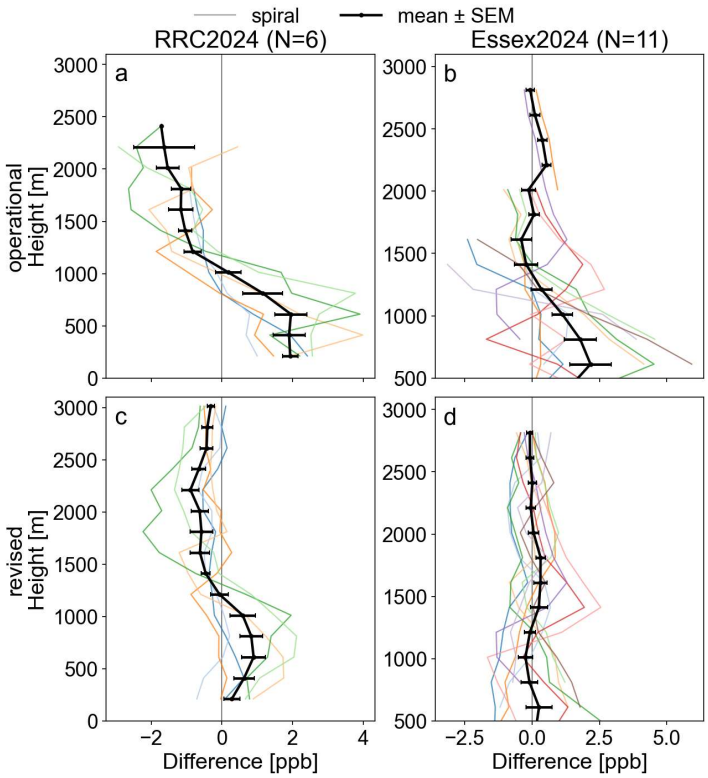


Figure 8. Mean Pandora−aircraft HCHO difference (± SEM) by height for: operational (a, b) vs. revised (c, d) height mapping, at the RRC and Essex sites in 2024. Due to the sampling limitations, altitudes<500 m were not used for difference calculations at Essex.

4 Conclusions

This study evaluates vertically resolved HCHO retrievals from Pandora MAX-DOAS observations against aircraft in situ measurements collected during the SARP East 2024 and 2025, and ALEGROS campaigns at multiple U.S. East Coast sites. Across 30 collocated spirals, Pandora tropospheric columns are consistent with aircraft-integrated columns within measurement uncertainty. Differences between Pandora and aircraft columns were within 1 standard deviation (combined uncertainty) for 60% of the spiral comparisons. Excluding the spirals at Essex, MD, 79% of the spirals yielded aircraft-based columns that met the 1 standard deviation threshold, while 100% of the spirals had column agreement within 2 standard deviations. Spatial and vertical representativeness appears to be a key factor controlling the quality of individual comparisons. Careful attention to viewing geometry is essential when interpreting agreements or discrepancies between Pandora and in situ observations.

A key finding of this work is that the retrieved vertical profile shapes can be significantly improved using a revised PZA-to-height mapping formulation. By reinterpreting the O_2–O_2 derived geometric proxy as an upper sensitivity bound rather than a layer midpoint, the revised approach distributes retrieved mixing ratios more consistently with the asymmetric, surface-weighted sensitivity structure of MAX-DOAS observations. We assert that this is a property of the mapping's underlying assumptions rather than of any one site or season, and the correction is expected to generalize beyond the sampled conditions. Comparison with aircraft profiles demonstrates that the revised Pandora profiles are in substantially better physical agreement (near-surface bias $\leq$ 0.7 ppb) with the in situ data than the operational mapping. We recommend adopting the revised height mapping in operational PGN retrievals, to avoid systematic concentration of the HCHO column into the lowest few retrieval layers. These recommendations were formalized by the PGN

into an ‘rfuh6’ data version, intended to supersede ‘rfuh5’, that is undergoing network-wide internal evaluation. Additional considerations and areas for improvement may be uncovered via this evaluation.

These results have direct implications for satellite validation. Pandora direct-sun and MAX-DOAS HCHO columns, combined with the MAX-DOAS profile shape, provide complementary constraints for evaluating geostationary retrievals from TEMPO and other satellite instruments. While column observations anchor the total burden, the profile shape can help inform the vertical distribution used in satellite air-mass factor calculations. Recent work has shown that NASA's GEOS Composition Forecast (GEOS-CF) model, which provides a priori inputs to TEMPO retrievals, significantly overestimates tropospheric HCHO columns over the Southeast and Northeast Coastal US, driven largely by errors in the modeled vertical distribution in the lower boundary layer (Zhao et al., 2025). The consistency of revised Pandora MAX-DOAS HCHO retrievals with independent aircraft data supports their use in diagnosing and reducing such errors.

Looking ahead, extending this evaluation to NO_2 presents additional challenges: NO_2 exhibits substantially stronger spatial heterogeneity near emission sources, making the path-integrated character of MAX-DOAS observations a more significant complication than for HCHO. In this work, we highlight the challenges in comparing path-integrated remote sensing measurements with point samples. A robust treatment of representativeness issues will likely require experimental designs that explicitly map horizontal structure rather than relying on point-to-path comparisons alone or limiting comparisons to regions that are more homogeneous.

Appendix A: Pandora MAX-DOAS retrieval

The following describes the mathematical formulation of the PGN MAX-DOAS profile retrieval. This appendix is provided for completeness; a high-level description of the retrieval logic is given in Sect. 2.1. The algorithm derives tropospheric columns, near-surface mixing ratios, and vertically resolved profiles from sequences of sky-scattered spectra using O_2–O_2 as an observational proxy for photon path length, without requiring explicit radiative transfer inversion.

A1. Photon path length from O_2–O_2

In the complete forward problem, each measured differential slant column (dSCD), at elevation angle θ, is an integral of the absorber concentration (n) weighted by a complex photon path distribution:

$$\mathrm{d}SCD(\theta,\lambda) = \int_0^\infty n(z)\ W(z;\theta,\lambda,\text{atmosphere})\ dz \tag{A1}$$

where the weighting function $W(z)$ depends on geometry, Rayleigh scattering, aerosols, surface reflectance, and multiple scattering. Rather than inverting measured differential slant column densities (dSCDs) through a full radiative transfer model, the algorithm uses O_2–O_2 (oxygen collision-induced absorption) as a direct observational proxy for effective photon path length: because the vertical distribution of O_2–O_2 is well-constrained by air density, measured O_2–O_2 dSCDs encode information about where in the atmosphere photons are scattered and how far they travel. The measured O_2–O_2 differential slant column can be approximated as:

$$\mathrm{d}SCD_{O_2O_2}(\theta) = \int_0^\infty n_{O_2O_2}(z)\ W(z;\theta)\ dz\ \approx\ n_{O_2O_2}^{\text{surface}}\, L_{\text{eff}}(\theta) \tag{A2}$$

where $L_{\text{eff}}(\theta)$is an effective photon path length. This approximation replaces the full radiative transfer kernel with a single scalar quantity per elevation angle.

A2. Tropospheric column

The tropospheric column (q) is estimated from trace gas observations at 75° zenith angle, with an O_2–O_2-derived effective AMF. If the 60° measurement is purely single scattering and artifact-free, its AMF from geometry ($1/\cos(60)$) is 2—then the denominator in the equation below reduces to $dSCD_{O_2O_2}(75)$. The AMF formulation in eq. A3 corrects the 75° observation by comparing the observation at 60° to a Rayleigh, single-scattering atmosphere:

$$q_{gas} = \frac{dSCD_{gas}(75)}{AMF(75)} = \frac{dSCD_{gas}(75)}{dSCD_{O_2O_2}(75) - dSCD_{O_2O_2}(60) + 2 * q_{O_2O_2,clim}}\, q_{O_2O_2,clim} \tag{A3}$$

A3. Profile shape prior

For the profile retrieval, dSCDs for the trace gas and O_2–O_2 are normalized to their respective tropospheric columns, to yield differential air mass factors (dAMFs):

$$dAMF = \frac{dSCD}{q} \tag{A4}$$

The Rayleigh-equivalent dAMF is computed from a pre-calculated lookup table.

A profile shape prior is constructed from the relative deviation of trace gas and O_2–O_2 dAMFs. If HCHO had the same vertical distribution as O_2–O_2, ($dAMF_{gas} - dAMF_{O_2O_2}$) would vanish; a nonzero residual encodes vertical structure relative to the O_2–O_2 profile. The denominator includes an empirical normalizing term that prevents collapse under Rayleigh-dominated conditions, and the numerator includes an empirically calibrated offset:

$$ps(\theta) = \frac{0.5 + dAMF_{gas}(\theta) - dAMF_{O_2O_2}(\theta)}{dAMF_{O_2O_2}(\theta) + 1}; \quad \text{(A5)}$$

The profile shape prior used in subsequent steps is normalized:

$$psn(\theta) = \frac{ps(\theta)}{\max(ps(\theta))} \quad \text{(A6)}$$

A4. O_2–O_2 reference and aerosol correction

The number density at each elevation angle is estimated by combining three contributions:

$$n_{gas}(\theta) \propto 2 \times Direct\ signal + 0.5 \times Aerosol\ correction - O_2O_2\ baseline \quad \text{(A7)}$$

The first term is simply the trace gas dSCD observation. The second estimates how much aerosol scattering has reduced the gas dSCD, derived from the deviation of the observed O_2–O_2 AMF from its Rayleigh value (from a precomputed look up table), and scaled by the trace gas tropospheric column:

$$Aerosol\ correction = [dAMF_{O_2O_2-Rayle}\ (\theta) - dAMF_{O_2O_2}(\theta)] \times q_{gas} \quad \text{(A8)}$$

The third removes the contribution that would exist even if the trace gas had the same profile as O_2–O_2, isolating the residual vertical structure:

$$O_2O_2\ baseline = dAMF_{O_2O_2}(\theta) \times q_{gas} \quad \text{(A9)}$$

Combining the above terms with the profile shape prior, and normalizing by the absolute O_2–O_2 slant column:

$$n_{gas}(\theta) = \frac{2dSCD_{gas}(\theta) + 0.5 \times [dAMF_{O_2O_2-Rayleigh}(\theta) - 3 \times dAMF_{O_2O_2}(\theta)]q_{gas}}{dSCD_{O_2O_2}(\theta) + q_{O_2O_2}} \times n_{O_2O_2}^{\text{surface}} \times psn(\theta) \quad \text{(A10)}$$

A5. Profile shape correction

The profile shape implied by n_{gas} is compared against the O_2–O_2 geometric prior *psn*. A correction factor is calculated as:

$$cf(\theta) = psn(\theta) - \frac{n_{gas}(\theta)}{\max(n_{gas}(\theta))} \quad \text{(A11)}$$

When *cf* is negative— indicating that the retrieved n_{gas} implies a more elevated profile shape than the O_2–O_2 geometry predicts — a downward correction is applied:

$$n_{gas}(\theta) = n_{gas}(\theta) \times [1 + cf(\theta)], where\ cf < 0 \quad \text{(A12)}$$

The intended purpose of this asymmetric correction is to suppress concentrations at upper layers that may reflect cloud contamination: if clouds enhance scattering aloft, n_{gas} would be inflated relative to the geometric prior.

A6. Column normalization

Negative n_{gas} values are set to zero. Partial columns are computed using the corresponding number density and layer width. Partial columns are then scaled to enforce closure with the independently retrieved tropospheric column q_{gas}.

A7. Near-surface mixing ratios

Near-surface trace gas mixing ratios are retrieved by extrapolating to a principal zenith angle of 90° — the horizon — from the largest available elevation angle, which is typically 89°. To account for variability in atmospheric mixing conditions, four concentration estimates are computed based on combinations of this extrapolated horizon value and the largest measured elevation angle, under both fully mixed and heterogeneous atmospheric assumptions. The largest value among these four estimates is selected as the reported surface concentration, along with a heterogeneity flag that characterizes the degree of vertical mixing near the surface. Details regarding heterogeneity flags are in Cede (2024).

Code and data availability

All data are publicly available online at the following locations:

SARP and ALEGROS airborne and ground in situ measurements:

https://www-air.larc.nasa.gov/cgi-bin/ArcView/sarp.2024

https://www-air.larc.nasa.gov/cgi-bin/ArcView/sarp.2025

Pandora operational data: http://data.pandonia-global-network.org

Custom Pandora retrievals used in the intercomparison:
https://dataverse.harvard.edu/dataset.xhtml?persistentId=doi:10.7910/DVN/NNZ0HB

HRRR data were accessed using the Python Herbie (Blaylock, 2026) tool.

Code available on request.

Author contributions

AP and TH designed Pandora observation strategies and collected ground in situ measurements, with support from RL and PZ. AP conducted the intercomparison analysis and devised the modified retrieval height mapping. GW, and ED designed flight plans; GW and JSC collected the CAFE data; and KT collected the TAMMS data. BP, JP and ES contributed valuable suggestions on analysis. AP prepared the manuscript with contributions from all co-authors.

Competing interests

At least one of the (co-)authors is a member of the editorial board of Atmospheric Measurement Techniques.

Acknowledgements

The authors thank Pandora instrument PIs and local operators for crucial instrument support: John Moisin, John Anderson, Lukas Valin. We also acknowledge intensive network operations support from Eric Baumann, Nicholas Lombel and Nader Abuhassan. We thank the EPA ACE program for funding the ALEGROS flights.

Financial support

This work was supported by NASA ROSES (80NSSC26K0077) and the NASA Tropospheric Composition Program.

References

Barrick, J. D. W., Ritter, J. A., Watson, C. E., Wynkoop, M. W., Quinn, J. K., and Norfolk, D. R.: Calibration of NASA Turbulent Air Motion Measurement System, 1996.

Blaylock, B. K.: Herbie: Retrieve Numerical Weather Prediction Model Data (2026.9.1), https://doi.org/10.5281/ZENODO.4567540, 2026.

Cede, A.: Manual for Blick Software Suite 1.8, 2024.

Chi, N. D. T., Tanimoto, H., Inomata, S., Fujinawa, T., Müller, A., and Sugita, T.: Characterization of Pandora sky-scan modes from the Japan Pandora Network and evaluation of their use in validating satellite NO2 and HCHO retrievals, ACS EST Air, 2, 2872–2888, https://doi.org/10.1021/acsestair.5c00223, 2025.

Choi, W. J.: Introducing the geostationary environment monitoring spectrometer, J. Appl. Remote Sens., 12, 1, https://doi.org/10.1117/1.JRS.12.044005, 2018.

De Smedt, I., Pinardi, G., Vigouroux, C., Compernolle, S., Bais, A., Benavent, N., Boersma, F., Chan, K.-L., Donner, S., Eichmann, K.-U., Hedelt, P., Hendrick, F., Irie, H., Kumar, V., Lambert, J.-C., Langerock, B., Lerot, C., Liu, C., Loyola, D., Piters, A., Richter, A., Rivera Cárdenas, C., Romahn, F., Ryan, R. G., Sinha, V., Theys, N., Vlietinck, J., Wagner, T., Wang, T., Yu, H., and Van Roozendael, M.: Comparative assessment of TROPOMI and OMI formaldehyde observations and validation against MAX-DOAS network column measurements, Atmos. Chem. Phys., 21, 12561–12593, https://doi.org/10.5194/acp-21-12561-2021, 2021.

Dowell, D. C., Alexander, C. R., James, E. P., Weygandt, S. S., Benjamin, S. G., Manikin, G. S., Blake, B. T., Brown, J. M., Olson, J. B., Hu, M., Smirnova, T. G., Ladwig, T., Kenyon, J. S., Ahmadov, R., Turner, D. D., Duda, J. D., and Alcott, T. I.: The High-Resolution Rapid Refresh (HRRR): An hourly updating convection-allowing forecast model. Part I: Motivation and system description, Weather Forecast., 37, 1371–1395, https://doi.org/10.1175/WAF-D-21-0151.1, 2022.

Frieß, U., Monks, P. S., Remedios, J. J., Rozanov, A., Sinreich, R., Wagner, T., and Platt, U.: MAX-DOAS O_4 measurements: A new technique to derive information on atmospheric aerosols: 2. Modeling studies, J. Geophys. Res. Atmos., 111, 2005JD006618, https://doi.org/10.1029/2005JD006618, 2006.

Frieß, U., Beirle, S., Alvarado Bonilla, L., Bösch, T., Friedrich, M. M., Hendrick, F., Piters, A., Richter, A., Van Roozendael, M., Rozanov, V. V., Spinei, E., Tirpitz, J.-L., Vlemmix, T., Wagner, T., and Wang, Y.: Intercomparison of MAX-DOAS vertical profile retrieval algorithms: studies using synthetic data, Atmos. Meas. Tech., 12, 2155–2181, https://doi.org/10.5194/amt-12-2155-2019, 2019.

Harkey, M., Holloway, T., Kim, E. J., Baker, K. R., and Henderson, B.: Satellite Formaldehyde to Support Model Evaluation, J. Geophys. Res. Atmos., 126, e2020JD032881, https://doi.org/10.1029/2020JD032881, 2021.

Herman, J., Cede, A., Spinei, E., Mount, G., Tzortziou, M., and Abuhassan, N.: NO_2 column amounts from ground-based Pandora and MFDOAS spectrometers using the direct-sun DOAS technique: Intercomparisons and application to OMI validation, J. Geophys. Res. Atmos., 114, 2009JD011848, https://doi.org/10.1029/2009JD011848, 2009.

Honninger, G.: Multi axis differential optical absorption spectroscopy, Atmos Chem Phys, 2004.

Liao, J., Hanisco, T. F., Wolfe, G. M., St. Clair, J., Jimenez, J. L., Campuzano-Jost, P., Nault, B. A., Fried, A., Marais, E. A., Gonzalez Abad, G., Chance, K., Jethva, H. T., Ryerson, T. B., Warneke, C., and Wisthaler, A.: Towards a satellite formaldehyde – in situ hybrid estimate for organic aerosol abundance, Atmos. Chem. Phys., 19, 2765–2785, https://doi.org/10.5194/acp-19-2765-2019, 2019.

582 Mouat, A. P., Siegel, Z. A., and Kaiser, J.: Evaluation of Aeris mid-infrared absorption (MIRA), Picarro
583 CRDS (cavity ring-down spectroscopy) G2307, and dinitrophenylhydrazine (DNPH)-based sampling for
584 long-term formaldehyde monitoring efforts, Atmos. Meas. Tech., 17, 1979–1994,
585 https://doi.org/10.5194/amt-17-1979-2024, 2024.

586 Nowak, S. N.: Remote Sensing of the Lower Atmosphere: From Surface Concentration to Mixing Layer
587 Height, Virginia Polytechnic Institue and State University, Blacksburg, VA, 2022.

588 Nowlan, C. R., Liu, X., Janz, S. J., Kowalewski, M. G., Chance, K., Follette-Cook, M. B., Fried, A.,
589 González Abad, G., Herman, J. R., Judd, L. M., Kwon, H.-A., Loughner, C. P., Pickering, K. E., Richter,
590 D., Spinei, E., Walega, J., Weibring, P., and Weinheimer, A. J.: Nitrogen dioxide and formaldehyde
591 measurements from the GEOstationary Coastal and Air Pollution Events (GEO-CAPE) Airborne Simulator
592 over Houston, Texas, Atmos. Meas. Tech., 11, 5941–5964, https://doi.org/10.5194/amt-11-5941-2018,
593 2018.

594 Ortega, I., Hannigan, J. W., Edwards, D., Stremme, W., Grutter, M., and Cadena-Caicedo, A.: Evaluating
595 TEMPO formaldehyde retrievals with co-located ground-based FTIR and Pandora observations, J.
596 Geophys. Res. Atmos., 131, e2026JD046497, https://doi.org/10.1029/2026JD046497, 2026.

597 Park, J.-U., Lim, S., Hanisco, T. F., Abuhassan, N., Place, B. K., Pandey, A., Cede, A., Tiefengraber, M.,
598 Gebetsberger, M., Park, J., Choi, J., Crawford, J. H., Song, C.-K., and Kim, S.-W.: Global analysis of
599 nitrogen dioxide and formaldehyde column densities from the Pandora global network: Variability and
600 implications for satellite validation, Remote Sens. Environ., 335, 115249,
601 https://doi.org/10.1016/j.rse.2026.115249, 2026.

602 Rawat, P., Crawford, J. H., Travis, K. R., Judd, L. M., Demetillo, M. A. G., and Valin, L. C.: Maximizing
603 the scientific application of Pandora column observations of HCHO and NO2, Atmos. Meas. Tech., 18,
604 2899–2917, https://doi.org/10.5194/amt-18-2899-2025, 2025.

605 Rawat, P., Travis, K. R., Henderson, B., Crawford, J. H., Judd, L. M., and Demetillo, M. A. G.:
606 Spatiotemporal assessment of the TEMPO formaldehyde column retrieval using the Pandonia global
607 network, J. Geophys. Res. Atmos., 131, e2025JD044788, https://doi.org/10.1029/2025JD044788, 2026.

608 Rees, D., Barnett, J. J., and Labitzke, K.: COSPAR International Reference Atmosphere: 1986. Pt. 2:
609 Middle atmosphere models, Adv. Space Res., 10, 1990.

610 Sebol, A., Wolfe, G. M., Canty, T., St. Clair, J., Delaria, E., Kaiser, J., Desai, N., Rollins, A., Waxman, E.,
611 Zuraski, K., Place, B., Pandey, A., Singh, A., Ring, A., Gatebe, C., and Dean-Day, J.: Evaluation of
612 Pandora HCHO and NO2 with airborne in situ observations, Atmos. Meas. Tech., 19, 5539–5552,
613 https://doi.org/10.5194/amt-19-5539-2026, 2026.

614 Sfendla, Y., Stavrakou, T., Müller, J.-F., Oomen, G.-M., Opacka, B., Danckaert, T., De Smedt, I., and
615 Lerot, C.: Global VOC emissions quantified from inversion of TROPOMI spaceborne formaldehyde and
616 glyoxal data, Atmos. Chem. Phys., 26, 733–767, https://doi.org/10.5194/acp-26-733-2026, 2026.

617 Shim, C., Wang, Y., Choi, Y., Palmer, P. I., Abbot, D. S., and Chance, K.: Constraining global isoprene
618 emissions with Global Ozone Monitoring Experiment (GOME) formaldehyde column measurements, J.
619 Geophys. Res. Atmos., 110, 2004JD005629, https://doi.org/10.1029/2004JD005629, 2005.

620 Shutter, J. D., Allen, N. T., Hanisco, T. F., Wolfe, G. M., St. Clair, J. M., and Keutsch, F. N.: A new laser-
621 based and ultra-portable gas sensor for indoor and outdoor formaldehyde (HCHO) monitoring, Atmos.
622 Meas. Tech., 12, 6079–6089, https://doi.org/10.5194/amt-12-6079-2019, 2019.

Sinreich, R., Merten, A., Molina, L., and Volkamer, R.: Parameterizing radiative transfer to convert MAX-DOAS dSCDs into near-surface box-averaged mixing ratios, Atmos. Meas. Tech., 6, 1521–1532, https://doi.org/10.5194/amt-6-1521-2013, 2013.

Spinei, E., Whitehill, A., Fried, A., Tiefengraber, M., Knepp, T. N., Herndon, S., Herman, J. R., Müller, M., Abuhassan, N., Cede, A., Richter, D., Walega, J., Crawford, J., Szykman, J., Valin, L., Williams, D. J., Long, R., Swap, R. J., Lee, Y., Nowak, N., and Poche, B.: The first evaluation of formaldehyde column observations by improved Pandora spectrometers during the KORUS-AQ field study, Atmos. Meas. Tech., 11, 4943–4961, https://doi.org/10.5194/amt-11-4943-2018, 2018.

St. Clair, J. M., Swanson, A. K., Bailey, S. A., and Hanisco, T. F.: CAFE: a new, improved nonresonant laser-induced fluorescence instrument for airborne in situ measurement of formaldehyde, Atmos. Meas. Tech., 12, 4581–4590, https://doi.org/10.5194/amt-12-4581-2019, 2019.

Szykman, J. and Liu, X.: Tropospheric Emissions Monitoring of Pollution (TEMPO) Project: Level 2 Science Data Product Validation Plan (SAO-DRD-11), , https://tempo.si.edu/documents, 2023.

Tirpitz, J.-L., Frieß, U., Hendrick, F., Alberti, C., Allaart, M., Apituley, A., Bais, A., Beirle, S., Berkhout, S., Bognar, K., Bösch, T., Bruchkouski, I., Cede, A., Chan, K. L., Den Hoed, M., Donner, S., Drosoglou, T., Fayt, C., Friedrich, M. M., Frumau, A., Gast, L., Gielen, C., Gomez-Martín, L., Hao, N., Hensen, A., Henzing, B., Hermans, C., Jin, J., Kreher, K., Kuhn, J., Lampel, J., Li, A., Liu, C., Liu, H., Ma, J., Merlaud, A., Peters, E., Pinardi, G., Piters, A., Platt, U., Puentedura, O., Richter, A., Schmitt, S., Spinei, E., Stein Zweers, D., Strong, K., Swart, D., Tack, F., Tiefengraber, M., Van Der Hoff, R., Van Roozendael, M., Vlemmix, T., Vonk, J., Wagner, T., Wang, Y., Wang, Z., Wenig, M., Wiegner, M., Wittrock, F., Xie, P., Xing, C., Xu, J., Yela, M., Zhang, C., and Zhao, X.: Intercomparison of MAX-DOAS vertical profile retrieval algorithms: studies on field data from the CINDI-2 campaign, Atmos. Meas. Tech., 14, 1–35, https://doi.org/10.5194/amt-14-1-2021, 2021.

Travis, K. R., Judd, L. M., Crawford, J. H., Chen, G., Szykman, J., Whitehill, A., Valin, L. C., Spinei, E., Janz, S., Nowlan, C. R., Kwon, H., Fried, A., and Walega, J.: Can Column Formaldehyde Observations Inform Air Quality Monitoring Strategies for Ozone and Related Photochemical Oxidants?, J. Geophys. Res. Atmos., 127, e2022JD036638, https://doi.org/10.1029/2022JD036638, 2022.

Veefkind, J. P., Aben, I., McMullan, K., Förster, H., De Vries, J., Otter, G., Claas, J., Eskes, H. J., De Haan, J. F., Kleipool, Q., Van Weele, M., Hasekamp, O., Hoogeveen, R., Landgraf, J., Snel, R., Tol, P., Ingmann, P., Voors, R., Kruizinga, B., Vink, R., Visser, H., and Levelt, P. F.: TROPOMI on the ESA Sentinel-5 Precursor: A GMES mission for global observations of the atmospheric composition for climate, air quality and ozone layer applications, Remote Sens. Environ., 120, 70–83, https://doi.org/10.1016/j.rse.2011.09.027, 2012.

Vigouroux, C., Langerock, B., Bauer Aquino, C. A., Blumenstock, T., Cheng, Z., De Mazière, M., De Smedt, I., Grutter, M., Hannigan, J. W., Jones, N., Kivi, R., Loyola, D., Lutsch, E., Mahieu, E., Makarova, M., Metzger, J.-M., Morino, I., Murata, I., Nagahama, T., Notholt, J., Ortega, I., Palm, M., Pinardi, G., Röhling, A., Smale, D., Stremme, W., Strong, K., Sussmann, R., Té, Y., Van Roozendael, M., Wang, P., and Winkler, H.: TROPOMI–Sentinel-5 Precursor formaldehyde validation using an extensive network of ground-based Fourier-transform infrared stations, Atmos. Meas. Tech., 13, 3751–3767, https://doi.org/10.5194/amt-13-3751-2020, 2020.

Wagner, T., Dix, B., Friedeburg, C. V., Frieß, U., Sanghavi, S., Sinreich, R., and Platt, U.: MAX-DOAS O_4 measurements: A new technique to derive information on atmospheric aerosols—Principles and information content, J. Geophys. Res. Atmos., 109, 2004JD004904, https://doi.org/10.1029/2004JD004904, 2004.

Wagner, T., Burrows, J. P., Deutschmann, T., Dix, B., Von Friedeburg, C., Frieß, U., Hendrick, F., Heue, K.-P., Irie, H., Iwabuchi, H., Kanaya, Y., Keller, J., McLinden, C. A., Oetjen, H., Palazzi, E., Petritoli, A.,

669 Platt, U., Postylyakov, O., Pukite, J., Richter, A., Van Roozendael, M., Rozanov, A., Rozanov, V.,
670 Sinreich, R., Sanghavi, S., and Wittrock, F.: Comparison of box-air-mass-factors and radiances for
671 Multiple-Axis Differential Optical Absorption Spectroscopy (MAX-DOAS) geometries calculated from
672 different UV/visible radiative transfer models, Atmos. Chem. Phys., 7, 1809–1833,
673 https://doi.org/10.5194/acp-7-1809-2007, 2007.

674 Wagner, T., Beirle, S., Brauers, T., Deutschmann, T., Frieß, U., Hak, C., Halla, J. D., Heue, K. P.,
675 Junkermann, W., Li, X., Platt, U., and Pundt-Gruber, I.: Inversion of tropospheric profiles of aerosol
676 extinction and HCHO and NO_2 mixing ratios from MAX-DOAS observations in Milano during the summer
677 of 2003 and comparison with independent data sets, Atmos. Meas. Tech., 4, 2685–2715,
678 https://doi.org/10.5194/amt-4-2685-2011, 2011.

679 Wolfe, G. M., Nicely, J. M., St. Clair, J. M., Hanisco, T. F., Liao, J., Oman, L. D., Brune, W. B., Miller, D.,
680 Thames, A., González Abad, G., Ryerson, T. B., Thompson, C. R., Peischl, J., McKain, K., Sweeney, C.,
681 Wennberg, P. O., Kim, M., Crounse, J. D., Hall, S. R., Ullmann, K., Diskin, G., Bui, P., Chang, C., and
682 Dean-Day, J.: Mapping hydroxyl variability throughout the global remote troposphere via synthesis of
683 airborne and satellite formaldehyde observations, Proc. Natl. Acad. Sci., 116, 11171–11180,
684 https://doi.org/10.1073/pnas.1821661116, 2019.

685 Zhao, T., Mao, J., Zhao, X., Pandey, A., Shah, V., Knowland, K. E., Kaiser, J., Tiefengraber, M.,
686 Gebetsberger, M., Cede, A., Spinei, E., and Hanisco, T. F.: Summertime Diurnal Variability of
687 Formaldehyde Over the Contiguous United States: Constraints From Pandonia Global Network, Geophys.
688 Res. Lett., 52, e2025GL116033, https://doi.org/10.1029/2025GL116033, 2025.

689 Zoogman, P., Liu, X., Suleiman, R. M., Pennington, W. F., Flittner, D. E., Al-Saadi, J. A., Hilton, B. B.,
690 Nicks, D. K., Newchurch, M. J., Carr, J. L., Janz, S. J., Andraschko, M. R., Arola, A., Baker, B. D.,
691 Canova, B. P., Chan Miller, C., Cohen, R. C., Davis, J. E., Dussault, M. E., Edwards, D. P., Fishman, J.,
692 Ghulam, A., Gonzalez Abad, G., Grutter, M., Herman, J. R., Houck, J., Jacob, D. J., Joiner, J., Kerridge, B.
693 J., Kim, J., Krotkov, N. A., Lamsal, L., Li, C., Lindfors, A., Martin, R. V., McElroy, C. T., McLinden, C.,
694 Natraj, V., Neil, D. O., Nowlan, C. R., O'Sullivan, E. J., Palmer, P. I., Pierce, R. B., Pippin, M. R., Saiz-
695 Lopez, A., Spurr, R. J. D., Szykman, J. J., Torres, O., Veefkind, J. P., Veihelmann, B., Wang, H., and
696 Wang, J.: Tropospheric emissions: Monitoring of pollution (TEMPO), J. Quant. Spectrosc. Radiat. Transf.,
697 186, 17–39, https://doi.org/10.1016/j.jqsrt.2016.05.008, 2017.

698